Brownian Dynamics and Molecular Dynamics Study of the Association between Hydrogenase and Ferredoxin from *Chlamydomonas reinhardtii*

Hai Long, Christopher H. Chang, Paul W. King, Maria L. Ghirardi, and Kwiseon Kim

National Renewable Energy Laboratory, Golden, Colorado

ABSTRACT   The [FeFe] hydrogenase from the green alga *Chlamydomonas reinhardtii* can catalyze the reduction of protons to hydrogen gas using electrons supplied from photosystem I and transferred via ferredoxin. To better understand the association of the hydrogenase and the ferredoxin, we have simulated the process over multiple timescales. A Brownian dynamics simulation method gave an initial thorough sampling of the rigid-body translational and rotational phase spaces, and the resulting trajectories were used to compute the occupancy and free-energy landscapes. Several important hydrogenase-ferredoxin encounter complexes were identified from this analysis, which were then individually simulated using atomistic molecular dynamics to provide more details of the hydrogenase and ferredoxin interaction. The ferredoxin appeared to form reasonable complexes with the hydrogenase in multiple orientations, some of which were good candidates for inclusion in a transition state ensemble of configurations for electron transfer.

INTRODUCTION

The photobiological generation of hydrogen gas by the green alga *Chlamydomonas reinhardtii* provides a promising pathway for renewable hydrogen production (1–7). The H$_2$-production process of *C. reinhardtii* is sensitive to O$_2$ (8). Although oxygenic photosynthesis and H$_2$ production would thus appear to be incompatible, it has been possible to find conditions under which the O$_2$ production activity of photosystem II (PSII) is decreased enough to induce hydrogenase activity. For instance, when the environmental sulfur supplies are limiting in sealed cultures, the rates of photosynthetic O$_2$ evolution decrease (9) and respiration rapidly consumes the remaining O$_2$, thereby creating an anaerobic environment (9–14). At the same time, the activity in photosystem I (PSI) is preserved and the photochemical energy absorbed by PSI is converted into electrochemical energy in the form of low-potential electrons that are transferred to soluble ferredoxins. Photooxidized PSI may be reduced by the chloroplastic quinone pool, which is in turn kept reduced by residual PSII activity as well as by some of the reducing equivalents originally stored as starch during sulfur-replete conditions (15–17). Thus, by alternating between conditions of sulfur exposure and deprivation, hydrogen gas can be produced in a sustainable way (11).

Optimizing this process to permit simultaneous water oxidation and proton reduction at high PSII and PSI activity would be desirable, and several challenges that would arise in such a system remain to be addressed. Among these is the multiplicity of partners for PSI-reduced ferredoxin under normal growth conditions, which include ferredoxin-NADP$^+$ reductase (FNR) to generate reductant for CO$_2$ fixation, and hydrogenase to generate hydrogen gas (7,18). The Michaelis-Menten constant (K_M) of FNR versus hydrogenase for reduced ferredoxin (FNR K_M values of 0.4 μM (19) versus hydrogenase K_M values of 10–35 μM (20,21)), suggests that the CO$_2$ fixation pathway through FNR might be a preferred electron sink to H$_2$ production. The electron flux through these two competing pathways is in part a function of the thermodynamic and kinetic parameters for the ferredoxin-dependent reduction of each enzyme. Since FNR is one of the central enzymes in the photosynthetic pathway, one long-term possibility to optimize biological hydrogen production is to engineer the hydrogenase-ferredoxin interaction to divert greater electron flux to this pathway. For this reason, and to better understand the mechanism of electron transfer between the [2Fe-2S] ferredoxin and hydrogenase, detailed information on how the hydrogenase interacts with the ferredoxin is required. Compared to the studies on interactions between FNR and ferredoxin (22–27), relatively few studies on the hydrogenase-ferredoxin interaction (18,20,21,28) exist and experimental data are limited. There are two hydrogenases (HydA1 and HydA2) (29) and at least six [2Fe-2S] ferredoxins (PetF1-PetF6) (30) encoded in the *C. reinhardtii* genome. Although structures for the hydrogenase and hydrogenase-ferredoxin complex from *C. reinhardtii* are still unknown, it is possible to use computational methods to build models. Chang et al. used homology modeling and rigid-body docking to simulate a hydrogenase (HydA2)-ferredoxin (PetF1) electron-transfer complex (31). Filtered by the intermetallocluster distance and refined by the potential energy calculation, two candidates for a hydrogenase-ferredoxin binding complex were identified, which in keeping with the previous work are referred to here by their original index numbers 16 and 42. Of these, complex 16 was determined to have a lower binding free energy. Therefore, complex 16 was suggested to more likely represent an in vivo

interacting configuration between the hydrogenase and ferredoxin during electron transfer (31).

The structures of the hydrogenase-ferredoxin complexes 16 and 42 are shown in Fig. 1. The major difference between these two structures is the orientation of the ferredoxin with respect to the hydrogenase. The two structures are related by an ~180° rotation of the ferredoxin around the axis from the $[4Fe4S]_H$ subcluster of the hydrogenase catalytic center H-cluster to the $[2Fe2S]_F$ cluster of the ferredoxin. The binding interface on the hydrogenase has many positively charged residues and the binding interfaces on the ferredoxin are mainly negatively charged, which is consistent with the role of charge-charge interaction in mediating formation of electron-transfer complexes (18). The detailed structures of the ferredoxin $[2Fe2S]_F$ cluster and H-cluster are shown in Fig. 2. The redox active $[2Fe2S]_F$ cluster of the ferredoxin functions as the electron carrier. During an electron-transfer event, the reduced ferredoxin binds to the hydrogenase and transfers a single electron to the hydrogenase H-cluster. The hydrogenase catalytic center H-cluster consists of a $[4Fe4S]_H$ cubane metallocluster and a $[2Fe]_H$ metallocluster. These two metalloclusters are covalently bonded together via a conserved cysteine (33). Two successive electron transfer events are required for a single catalytic cycle by the hydrogenase to produce one molecule of hydrogen gas.

Brownian dynamics (BD) has been widely used in recent years to study the protein association process (34–40). In most BD simulations, proteins are treated as rigid bodies and are moved by the Brownian forces stochastically (41). The long-range electrostatic force and desolvation effects are considered, whereas short-range interactions such as hydrogen bonding, van der Waals forces, and explicit salt bridges, are neglected. Simplifying the force treatment gives the BD method the ability to simulate molecules over microsecond timescales within reasonable computational time. The BD simulation method has successfully reproduced experimentally measured protein association rates (36,42,43), as well as the transient encounter complexes during the association process (44). A free energy landscape analysis method based on the BD simulation trajectories was developed recently to

identify encounter complexes and to detail reaction pathways (45–47). When the two proteins are closer, however, short-range interactions become important. Therefore, more detailed (but slower) molecular dynamics (MD) simulations are required to simulate the dynamics of the encounter complex.

Based on the structures of complexes 16 and 42, we investigated the dynamics of the ferredoxin PetF1 association with the hydrogenase HydA2 using BD and all-atom MD simulations. Free energy landscapes were computed from BD trajectories, and the reaction pathways, as well as the encounter complexes, were identified. The details of the association dynamics in the encounter complexes were further characterized by atomistic MD.

METHODS

Reference structures

Based on the model structures of *C. reinhardtii* hydrogenase-ferredoxin complexes 16 and 42 (31), we ran BD and MD simulations with the hydrogenase in the oxidized state and the ferredoxin in both reduced and oxidized states. The CHARMM22 atomic charges and atom radii (48) were used for the amino acid residues of the hydrogenase and the ferredoxin in electrostatic potential calculations and MD simulations. The partial atomic charges and radii for the metalloclusters were derived from geometry-optimized model clusters, using a BLYP/6-31+G(d) model chemistry and Natural Population Analysis charges (49) (manuscript in preparation). We note that although this charge derivation procedure differs from the canonical CHARMM method, Meuwly and Karplus have found key dynamical features around the [3Fe4S] cluster of the *Azotobacter vinelandii* 7Fe ferredoxin insensitive to the particular charge model (50).

In the reduced state, the ferredoxin $[2Fe2S]_F$ cluster and the accompanying four cysteine sulfur ligands (from Cys_F^{39}, Cys_F^{44}, Cys_F^{47}, and Cys_F^{77}) have a total partial charge of -3, whereas in the oxidized state the total partial charge is -2. In this research, we assumed that the conformations of the reduced and oxidized ferredoxin were identical except for the peptide bond between residues Cys_F^{44} and Ser_F^{45}. In the oxidized state, Cys_F^{44}-CO points to the $[2Fe2S]_F$ cluster, whereas in the reduced state, the Cys_F^{44}-CO points away because of larger charge repulsion (Fig. 3) as reported by Morales et al. (51) The pK_a values of the charged residues on the reduced and oxidized ferredoxin were calculated using H++ (52,53). We found that the redox state of the $[2Fe2S]_F$ cluster had a very weak influence on the pK_a values and the protonation states of the charged residues on the ferredoxin remained the same at different $[2Fe2S]_F$ redox states at pH 7.0 (Supplementary Material, Table S1, Data S1). For the hydrogenase, we only simulated the hydrogenase
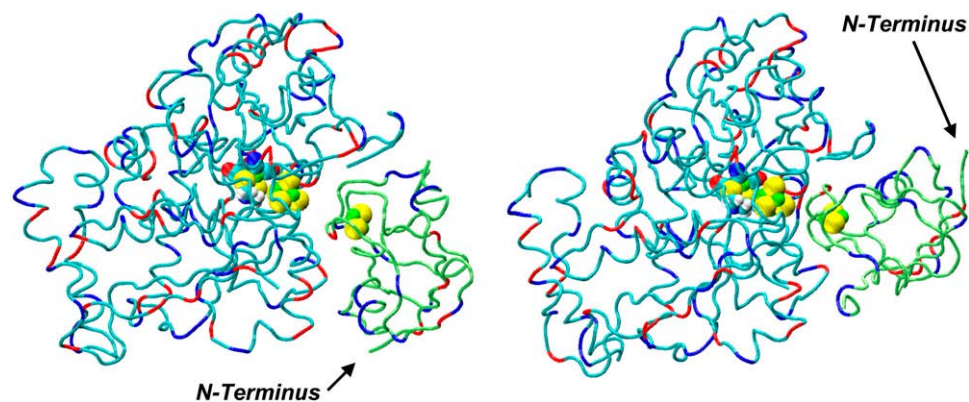

FIGURE 1 Structures of complex 16 (*left*) and complex 42 (*right*). Neutral residues of the hydrogenase are in cyan and those of the ferredoxin in lime green. The metalloclusters shown are the hydrogenase H-cluster and the ferredoxin $[2Fe2S]_F$ cluster. Positively charged residues on both proteins are shown in red, and negatively charged residues in blue. The pictures in Figs. 1–4 and 11, and in Table 2, were generated by VMD (32).
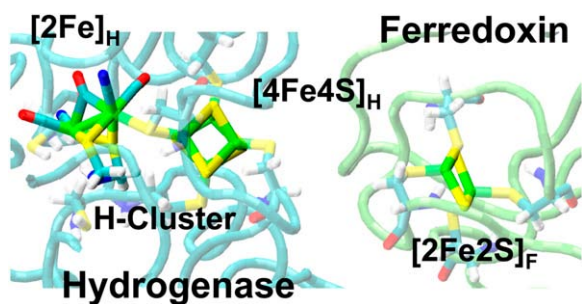
FIGURE 2 Detailed structures of the ferredoxin $[2Fe2S]_F$ cluster and the $[4Fe4S]_H$ and $[2Fe]_H$ clusters of the hydrogenase in complex 16.

with the H-cluster in the oxidized state. The total partial charge on the $[2Fe]_H$ cluster is -1, and the $[4Fe4S]_H$ cluster, along with the four cysteine sulfur ligands (from Cys_H^{111}, Cys_H^{166}, Cys_H^{366}, and Cys_H^{370}), has a total partial charge of -2.

Brownian dynamics simulations

We used the Brownian dynamics simulation program package Simulation of Diffusional Association (SDA) (54) to perform the BD simulations. We simulated a total of four systems: $BD16_R$, the atomic coordinates of the hydrogenase and ferredoxin from the energy-minimized structure of complex 16, with the ferredoxin in the reduced state; $BD16_O$, based on the complex 16 structure with an oxidized ferredoxin; $BD42_R$, based on the complex 42 structure with a reduced ferredoxin; and $BD42_O$, based on the complex 42 structure with an oxidized ferredoxin. During the BD simulation, both hydrogenase and ferredoxin were treated as rigid bodies. The center of mass (COM) of the hydrogenase was fixed in the center of the simulation sphere, and rotational movement was allowed. The ferredoxin moved stochastically
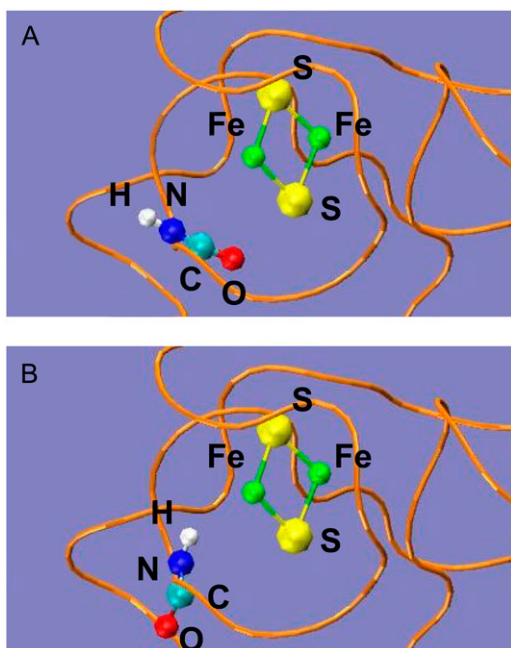

FIGURE 3 Conformational switch in the peptide bond between Cys_F^{44} and Ser_F^{45} for the oxidized (A) and reduced ferredoxin (B). The $[2Fe2S]_F$ cluster and the -C(=O)NH- peptide bond between the two residues are in CPK format, and the ferredoxin backbone is in tube format.

around the hydrogenase both translationally and rotationally. The BD simulations started at $b = 100$ Å of COM-COM distance between the hydrogenase and ferredoxin, and were terminated if the two proteins achieved a COM-COM distance of $c > b$. To improve the sampling statistics in the region close to the hydrogenase for the free energy landscape analysis, we used a small $c = 120$ Å. The BD simulations were performed at 50 mM, 150 mM, 300 mM, and 500 mM. At each ionic strength, 50,000 trajectories were generated.

The electrostatic interactions during the simulation were calculated using the following method. First, the electrostatic potential grid around each protein was calculated using the Adaptive Poisson-Boltzmann Solver (APBS) program (55) to solve the full Poisson-Boltzmann equation at the given ionic strength. The grid was centered at each protein and had a dimension of $161 \times 161 \times 161$ with a spacing size of 1 Å, as required by the SDA program. The solvent dielectric constant, ε_s, was 78.5 and the protein interior dielectric constant, ε_p, was set to 4.0. For details of the APBS calculation parameters, please refer to the sample APBS input file (Supplementary Material, Table S2, Data S1). Next, the effective charges on each protein were calculated by the ECM (Effective Changes for Macromolecules in solvent) module (56) in the SDA package. The effective charges are fitted to reproduce the molecular electrostatic potentials calculated by APBS. Finally, the charge desolvation penalty grid was calculated using the mk_ds_grd program in the SDA package (54). The desolvation energy for ferredoxin due to the presence of hydrogenase was computed according to

$$\Delta G_{ds} = \alpha \frac{\varepsilon_s - \varepsilon_p}{\varepsilon_s(2\varepsilon_s + \varepsilon_p)} \sum_{ij}(1 + \kappa r_{ij})^2 \exp(-2\kappa r_{ij}) \frac{q_i^2 a_j^3}{r_{ij}^4}, \quad (1)$$

where α is the scaling factor and we used a value of 1.67 from Gabdoulline and Wade (42); κ is the Debye-Hückel screening parameter, which depends on the given ionic strength; i and j denote atom i of the ferredoxin and atom j of the hydrogenase, respectively; q is the effective charge; a is the atomic radius; and r_{ij} is the distance between the two atoms. The desolvation energy for the hydrogenase due to the presence of the ferredoxin was computed in a similar way. During the BD simulation, the electrostatic interaction on the hydrogenase (or ferredoxin) was then computed using the effective charges on the hydrogenase (or ferredoxin) and the electrostatic potential grid of the ferredoxin (or hydrogenase). The charge desolvation penalty was calculated similarly using the effective charges and desolvation penalty grids. In this way, the energies could be evaluated much more quickly.

The BD trajectory was propagated by solving the diffusion equations. The translational diffusion equation is

$$\Delta \vec{r}(t) = \frac{D\Delta t}{k_B T}\vec{F}(t) + \vec{R}(t), \quad (2)$$

where D is the relative translational diffusion constant, Δt is the time step, $\vec{F}(t)$ is the instantaneous systematic potential force, k_B and T are the Boltzmann constant and temperature, respectively ($T = 298$ K in this work), and $\vec{R}(t)$ is the random displacement due to the collisions between the protein and the solvent molecules. The values of $\vec{R}(t)$ satisfy the boundary conditions

$$\langle \vec{R}(t) \rangle = 0 \quad \text{and} \quad \langle \vec{R}(t)\vec{R}(0) \rangle = 6D\Delta t. \quad (3)$$

The rotational diffusion equations for both hydrogenase and ferredoxin were solved in a similar way. The translational and rotational diffusion constants for the hydrogenase and ferredoxin were calculated by the program HYDROPRO (57) and the results are presented in Table 1. The calculated diffusion constants are similar to the diffusion constants of similarly sized proteins (42).

The BD simulation time step Δt was chosen as 1.0 ps when the COM-COM distance of the two proteins was within 80 Å. Since the relative translational diffusion constant, D, of the ferredoxin versus the hydrogenase is ~0.02 Å²/ps, the average movement per step is only $\sqrt{6D\Delta t} = 0.35$Å. At larger separation distances, Δt was increased linearly with a slope of 0.5 ps/Å.

	Complex 16	Complex 42
Relative translational diffusion constant (Å^2/ps)	2.160×10^{-2}	2.165×10^{-2}
Rotational diffusion constant of ferredoxin (rad^2/ps)	3.016×10^{-5}	2.937×10^{-5}
Rotational diffusion constant of hydrogenase (rad^2/ps)	5.918×10^{-6}	6.289×10^{-6}

Free energy landscape calculations

The free energy landscape calculation process is similar to that used by Spaar et al. (46,47). The trajectories of the BD simulations, along with the potential energy information, were stored and used for the free energy landscape calculations. To obtain the free energy, however, the entropy must be calculated. The entropy depends on the spatial and orientational distributions of the ferredoxin, which can be computed from the occupancy landscapes. For that reason, the free energy landscape was computed in three steps. First, the BD simulation trajectories were used to create the spatial and orientational occupancy landscapes of the ferredoxin. Second, from the occupancy landscapes, local entropy-loss landscapes were computed. Finally, based on the entropy-loss landscapes and the potential energy information in the trajectories, the free energy landscape was generated.

The computation of the spatial occupancy landscape

To analyze the BD trajectories of BD16_R and BD16_O, a reference coordinate system was constructed based on the bound structure of complex 16 (Fig. 4 A). The origin of the reference coordinate system was at the COM of the hydrogenase in the complex. The z axis direction points to the COM of the ferredoxin. Without loss of generality, the y axis direction was assigned as the normal vector of the plane that included the two COMs and the N-terminal nitrogen (N1) of the hydrogenase. For analyzing BD42_R and BD42_O trajectories, a similar reference coordinate system was constructed based on the bound structure of complex 42.

The coordinates from the BD trajectories were then transformed to new coordinates under the reference coordinate system. Since in the reference coordinate system the COM of the hydrogenase was at the origin, the COM-COM vector $\mathbf{r}_{\text{spatial}}(t)$ was the coordinates of the ferredoxin COM under the reference coordinate system. The length, r, zenith angle, θ_{spatial}, and azimuthal angle, ϕ_{spatial}, of the vector $\mathbf{r}_{\text{spatial}}(t)$ (Fig. 4 B) were then calculated so that they could be assigned into a 3-dimensional spherical grid accordingly. The grid spacing was $\Delta r = 2$ Å, $\Delta \theta_{\text{spatial}} = 2°$, and $\Delta \phi_{\text{spatial}} = 2°$. For the original bound-state structure, $\theta_{\text{spatial}} = 0$. By counting the occurrence of the ferredoxin COM in each grid bin, the spatial occupancy landscape of the ferredoxin was generated. The three-dimensional spherical grid is visualized as polar azimuthal-equidistant projections of half-spherical positive-z shells, each pertaining to a given COM-COM distance, R, using OpenDX (58). The negative-z half-sphere is not shown, as this corresponds to the hydrogenase surface opposite to the metallocluster binding sites, and no major occupancy above background was observed there.

The computation of the orientational occupancy landscape

The reference coordinate system used in the orientational occupancy landscape computation was the same as the one used to compute the spatial occupancy landscape (Fig. 4 B). However, for the orientational occupancy landscape computations, the vectors $\mathbf{r}_{\text{spatial}}(t)$ and $\mathbf{r}_{\text{orient}}(t)$ were both calculated. The $\mathbf{r}_{\text{orient}}(t)$ was defined as a vector pointing toward the COM of the ferredoxin from the COM of a virtual hydrogenase, placed according to the original bound state (Fig. 4 C). In this way, the zenith angle, θ_{orient}, and azimuthal angle, ϕ_{orient}, of vector $\mathbf{r}_{\text{orient}}(t)$ represent the angular orientation of

the ferredoxin in the global coordinate system at each point during the simulation. Visual orientation landscapes (e.g., Fig. 5 B) were polar azimuthal-equidistant projections of the positive-z half-sphere in the reference frame shown in Fig. 4 A, color-coded according to the accumulated (θ, ϕ) occupancy. Since the length of $\mathbf{r}_{\text{orient}}(t)$ was fixed, the length of $\mathbf{r}_{\text{spatial}}(t)$, along with the θ_{orient} and ϕ_{orient} angles of $\mathbf{r}_{\text{orient}}(t)$, was used to assign $\mathbf{r}_{\text{orient}}(t)$ to a 3-dimensional spherical grid similar to the one described in the previous section.

The computation of the local entropy-loss landscapes

The local entropy-loss landscape was computed using the method described by Spaar et al. (46,47). The local entropy loss is the sum of the translational (ΔS_{trans}) and rotational (ΔS_{rot}) entropy loss. The ΔS_{trans} landscape was also a 3-dimensional spherical grid. The ΔS_{trans} value at bin (r_0, θ_0, ϕ_0) could be calculated from the spatial occupancy landscape using the equation

$$\Delta S_{\text{trans}} = -k_B \sum_{n=1}^{N} P_n \ln P_n - k_B \ln N, \qquad (4)$$

where P_n is the probability at bin n in the spatial occupancy landscape and N is the number of spatial occupancy bins within the locally accessible volume, V. The accessible volume, V, was defined as a sphere around the spatial occupancy bin at (r_0, θ_0, ϕ_0) with a radius, R_{cut}, of 3 Å, the same value used by Spaar et al. (46). The error bars of ΔS_{trans} were estimated by varying R_{cut} from 2 Å to 4 Å. Similarly, the ΔS_{rot} landscape could also be computed with a rotational volume of $\theta_0 \pm 3°$ and $\phi_0 \pm 3°$, and the error bars were estimated by varying the rotational volume from $\theta_0 \pm 2°$ and $\phi_0 \pm 2°$ to $\theta_0 \pm 4°$ and $\phi_0 \pm 4°$.

The computation of the total energy and free energy landscapes

The total energy, ΔE, was calculated by

$$\Delta E = \Delta E_{\text{el}} + \Delta G_{\text{ds}}, \qquad (5)$$

where ΔE_{el} is the electrostatic potential energy and ΔG_{ds} is the desolvation energy, both of which can be obtained directly from the BD simulation trajectories. In the total energy landscapes, the ΔE value stored at bin (r_0, θ_0, ϕ_0) was the minimum value throughout the simulation trajectories at this position. In this way, we could identify the minimum free energy path (reaction path) of the hydrogenase-ferredoxin association dynamics. Finally, the free energy landscape could be computed by the equation

$$\Delta G = \Delta E - T\Delta S, \Delta S = \Delta S_{\text{trans}} + \Delta S_{\text{rot}}. \qquad (6)$$

Molecular dynamics simulations

The association dynamics of PetF1-HydA2 encounter complexes, the structures of which are illustrated in Table 2, were simulated with atomistic MD. Each encounter complex was solvated in a TIP3P water box. The water box was chosen to be large enough so that the protein atoms were at least 10 Å away from the box edges. Na^+ ions were added to neutralize the negative charges of the system. The MD simulations were performed using the NAMD simulation package (59) with the CHARMM22 protein force field (48). The time step used in the simulations was 1 fs. Electrostatic energies were calculated by the particle mesh Ewald summation method with ~1 Å mesh density. The simulated system was first minimized for 1000 steps using the conjugate gradient method. It was then equilibrated for 25 ps in the isothermal-isobaric (NPT) ensemble at 298 K and 1 atmosphere with all protein atoms fixed, followed by another 1000-step conjugate gradient minimization. The system was equilibrated for another 25 ps with only the protein backbone atoms fixed, followed by another minimization. Finally, the whole system was allowed to move and the production run began. Pro-
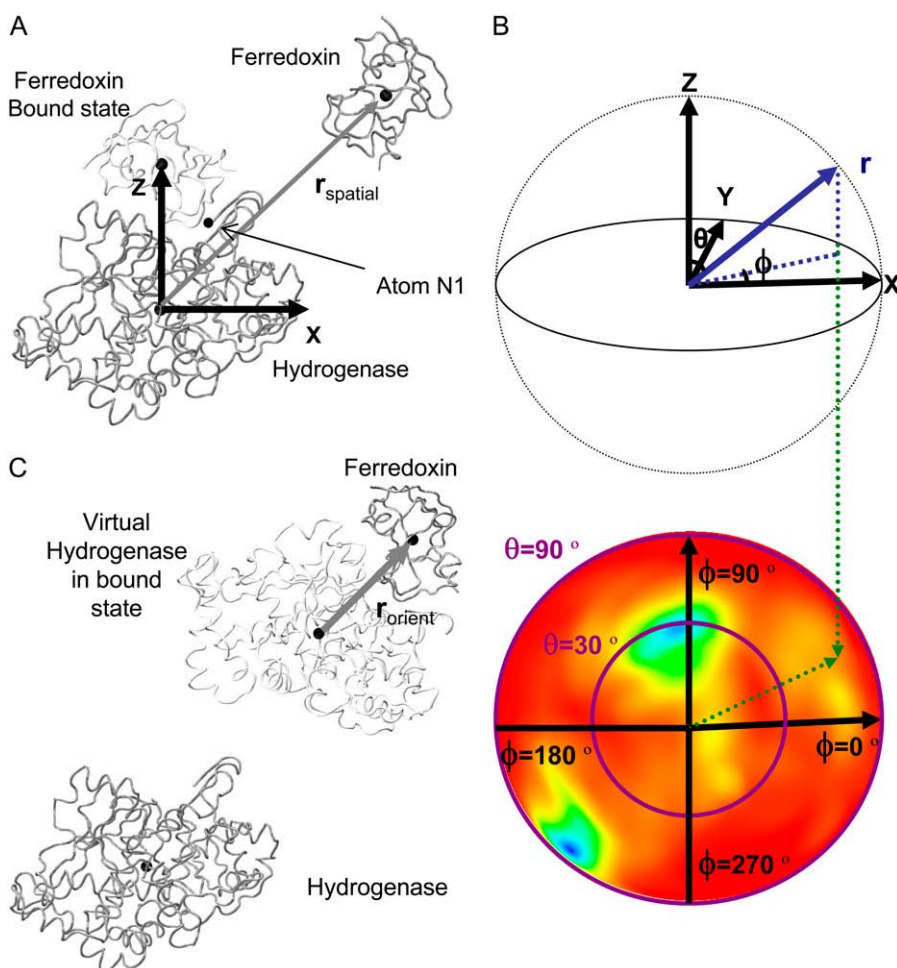
FIGURE 4 (A) Definition of the reference coordinate system and the $\mathbf{r}_{spatial}$ vector for $BD16_{R/O}$. (B) Definition of the zenith angle, θ, and azimuthal angle, ϕ, for $BD16_{R/O}$. (C) Definition of the $\mathbf{r}_{orient}$ vector for $BD16_{R/O}$.

duction runs were again done in the NPT ensemble with temperature coupled to a 298 K Langevin bath and pressure maintained at 1 atmosphere with a Langevin piston (60,61). The total simulation time for each encounter complex was 3 ns. For all simulations, trajectories were saved every 1 ps of simulation time for further analysis.

RESULTS

Occupancy landscapes

The spatial and orientational occupancy landscapes for $BD16_R$ at 50 mM ionic strength are displayed in Fig. 5. The COM-COM distance for the occupancy landscapes shown is 36 Å, at which distance the global minimum of the free energy occurs (see ''Free-energy landscapes'', below). For the spatial occupancy landscape (Fig. 5 A), the most frequently occupied position is close to the center of the map (where $\theta_{spatial} = 0°$), i.e., the position of the ferredoxin center in the original bound state. The orientational occupancy landscape at 36 Å (Fig. 5 B) has two major minima, showing that the ferredoxin orientational distribution is more diversified than its spatial distribution. Here, we define the edge-to-edge distance for a certain configuration, which is the closest distance between the hydrogenase $[4Fe4S]_H$ sulfur ligands

and the ferredoxin $[2Fe2S]_F$ sulfur ligands. For the minimum at the upper left of the map, when the two proteins are <36 Å from each other, the configuration at this minimum evolves into a configuration similar to the bound state, which has the smallest edge-to-edge distance during the simulation. We denote this configuration as encounter complex $EC16A_R$. For the other minimum at the lower left corner of the map, it represents a configuration that has the lowest free energy during the BD simulations as revealed by the free energy landscape analysis. We denote this configuration as $EC16B_R$. The occupancy landscapes for $BD16_O$ are similar (Supplementary Material, Fig. S1, Data S1).

The analogous landscapes for $BD42_R$ at 50 mM ionic strength are displayed in Fig. 6. The COM-COM distance for these landscapes is 40 Å, the distance corresponding to the global minimum of the free energy. As with $BD16_R$, in the spatial-occupancy landscape (Fig. 6 A) the most frequently occupied position is close to the center of the map. The orientational occupancy landscape (Fig. 6 B) has two major minima located in the left region of the map. The upper minimum is where the global free energy minimum occurs, denoted as $EC42B_R$. The second minimum is in the lower left corner, denoted as $EC42C_R$. As with $BD16_R$, we denote the
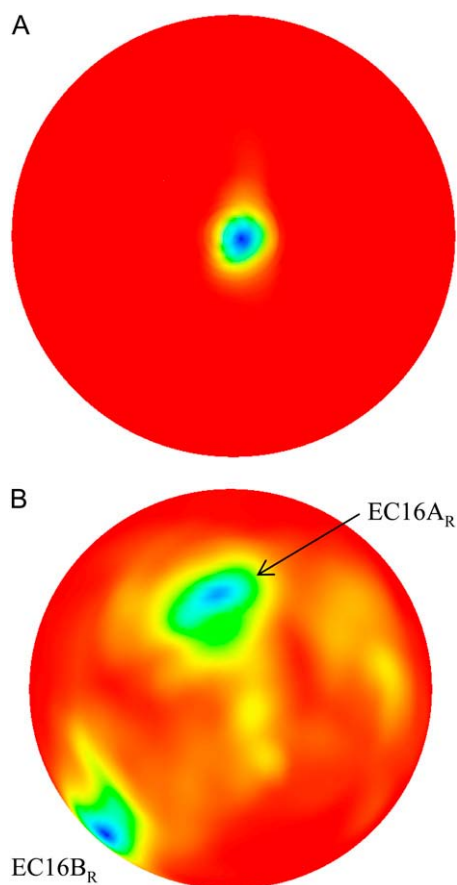
FIGURE 5 Spatial (*A*) and orientational (*B*) occupancy landscapes for BD16$_R$ at 50 mM ionic strength and a COM-COM distance of 36 Å. The color maps in Figs. 5–7 show low free energy areas as blue and high free energy areas as red. The models in Figs. 5–7 and in Supplementary Material (Data S1) were created by OpenDX (58).

configuration with the minimum edge-to-edge distance during the BD simulation as EC42A$_R$. EC42A$_R$ is close to the configuration in the bound state and occurs only when the two proteins are very close ($\leq$36 Å). The occupancy landscapes for BD42$_O$ are similar (Supplementary Material, Fig. S2, Data S1).

The encounter complexes identified above at 50 mM ionic strength are summarized in Table 2, with their free energies and configurations displayed. The same analysis was performed for all four systems at higher ionic strengths, and the configurations were found to be similar to those at 50 mM ionic strength for most of the systems. The lack of configuration changes with increasing ionic strength may be due to the close distances between the interacting charges resulting in weak ionic screening. The exception is EC42B$_{R/O}$: with increasing ionic strength, the ferredoxin moved slightly to adjust to the influence of the ionic strength change (Supplementary Material, Fig. S3, Data S1). This motion of the ferredoxin reduces the distance between the negatively charged residues Asp$_H^5$ and Glu$_F^{93}$ considerably and thus increases the free energy. The redox state of the ferredoxin also

has little influence on the configurations, which can be observed in Table 2. This indicates that the electrostatic interactions between the hydrogenase and ferredoxin are very strong in the encounter complexes, so that the redox state of the ferredoxin only has a modest influence on the shape of the free energy surface. Another interesting fact is that EC16B$_{R/O}$ and EC42C$_{R/O}$ are similar, but mutually different from both reference model complexes 16 and 42. Thus, the common configurations reported here may represent a third productive family of configurations for electron transfer.
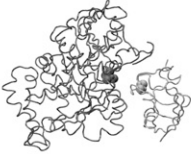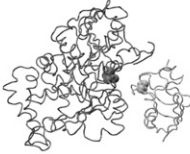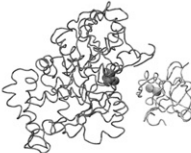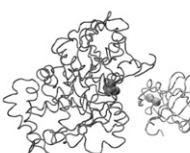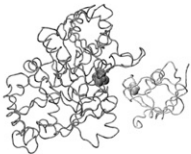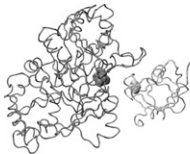
Free energy landscapes

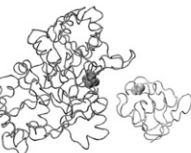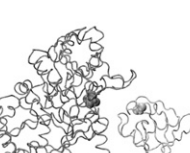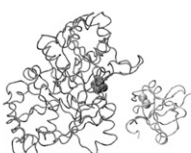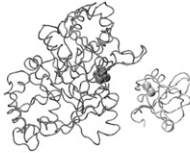The free energy landscapes at 36 Å and 40 Å for BD16$_R$ are shown in Fig. 7. When the two proteins are separated at a distance of 40 Å, the local free energy minimum is located near the center of the map. At a distance smaller by 4 Å, the local free energy minimum remains in the central region. However, as the local free energy minimum decreases in value, the basin area around the minimum gets more focused, showing that the degrees of freedom of the ferredoxin are more restricted when the two proteins are closer to each other. This is consistent with the funnel-shaped free energy landscapes found in other protein-protein association studies (45,46,62). The free energy landscapes for BD16$_O$, BD42$_R$, and BD42$_O$ are similar (Supplementary Material, Figs. S4–S6, Data S1).

The reaction path is defined as the path along the local minima of the free energy landscapes at different hydrogenase-ferredoxin separation distances. The free energy curve along the reaction paths for BD16$_R$ at 50 mM ionic strength is shown in Fig. 8 *A*. The electrostatic potential energy, desolvation energy, and entropy contributions to the free energies are shown in Fig. 8, *B–D*, respectively. Since only the local minimum energies are stored in the total energy landscape, there are no error bars for the electrostatic potential energy curve and the desolvation energy curve. The free energy error bars are from the entropy error bars and are too small to show on the free energy curve. The dominant contribution to the free energy is the electrostatic potential energy term. The contribution from the desolvation energy term is negligible by comparison. The entropy contribution is also trivial when the two proteins are far apart, and it becomes more significant when the two proteins approach each other, which is due to the greater loss of translational and rotational freedom when they are close.

The free energies along the reaction paths at different ionic strengths for BD16$_R$, BD16$_O$, BD42$_R$, and BD42$_O$ are shown in Fig. 9. For all BD simulation systems, when the distance between the hydrogenase and ferredoxin is ~80 Å, the interaction free energies are close to 0. Thus, the electrostatic interactions between the hydrogenase and ferredoxin are weak at large distances, and the ferredoxin rigid-body motion is much less restricted than at closer interprotein distances. The free energy becomes more negative as they become

TABLE 2 Names, free energies, and configurations of the encounter complexes derived from BD simulations at 50 mM ionic strength

| Reduced ferredoxin		Oxidized ferredoxin		Note
$EC16A_R$ -20.6 kcal/mol		$EC16A_O$ -20.0 kcal/mol		Minimum edge-to-edge distance
$EC16B_R$ -25.5 kcal/mol		$EC16B_O$ -22.4 kcal/mol		Lowest free energy
$EC42A_R$ -15.1 kcal/mol		$EC42A_O$ -12.1 kcal/mol		Minimum edge-to-edge distance
$EC42B_R$ -23.1 kcal/mol		$EC42B_O$ -21.8 kcal/mol		Lowest free energy
$EC42C_R$ -20.2 kcal/mol		$EC42C_O$ -18.5 kcal/mol		An important encounter complex in $BD42_{R/O}$

A

B

EC42B_R

EC42C_R
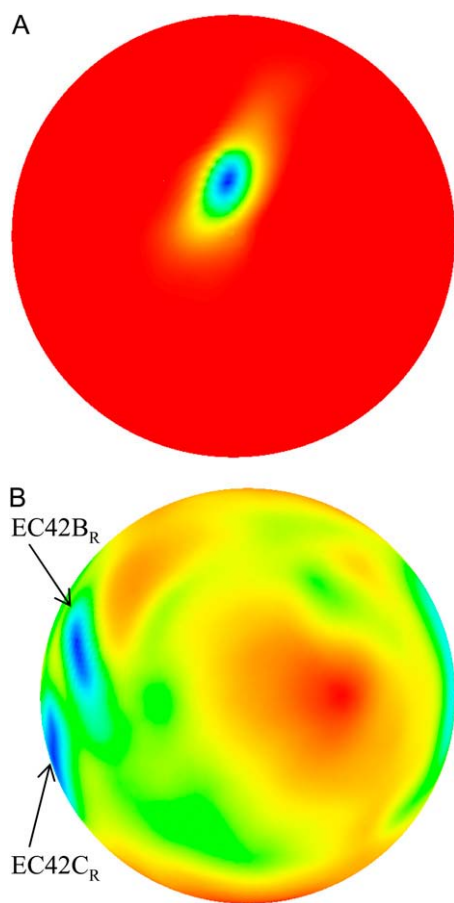
FIGURE 6 Spatial (*A*) and orientational (*B*) occupancy landscapes for BD42_R at 50 mM ionic strength and a COM-COM distance of 40 Å.

A

B

FIGURE 7 Free energy landscapes at 36 Å (*A*) and 40 Å (*B*) for BD16_R.

closer, illustrating the dominance of the electrostatic interaction. For all ionic strengths, the free energies reach minima at a distance of 40 Å for BD42_{R/O} and 36 Å for BD16_{R/O}. At 50 mM ionic strength, the global free energy minima are -25.5 kcal/mol for BD16_R, -23.1 kcal/mol for BD42_R, -22.4 kcal/mol for BD16_O, and -21.8 kcal/mol for BD42_O. The free energy minima of BD16/42_R are lower than those of BD16/42_O. This can be explained by the greater negative charge on the reduced ferredoxin, which attracts more strongly the positively charged binding interface on the hydrogenase. At the same ionic strength, the free energy minima of BD16_{R/O} are both more negative and at a smaller distance than those of BD42_{R/O}, suggesting that the configurations based on complex 16 may play a more important role than the configurations based on complex 42 during the ferredoxin-hydrogenase association.

The ionic strength has little influence on the calculated values of the free energy minima. Generally, we observe a slight negative correlation between ionic strength and the magnitude of free energy minima, as expected due to the weaker electrostatic attraction at higher ionic strengths. In addition, if other conditions are the same, the shapes of the free energy plots with different redox states of the ferredoxin
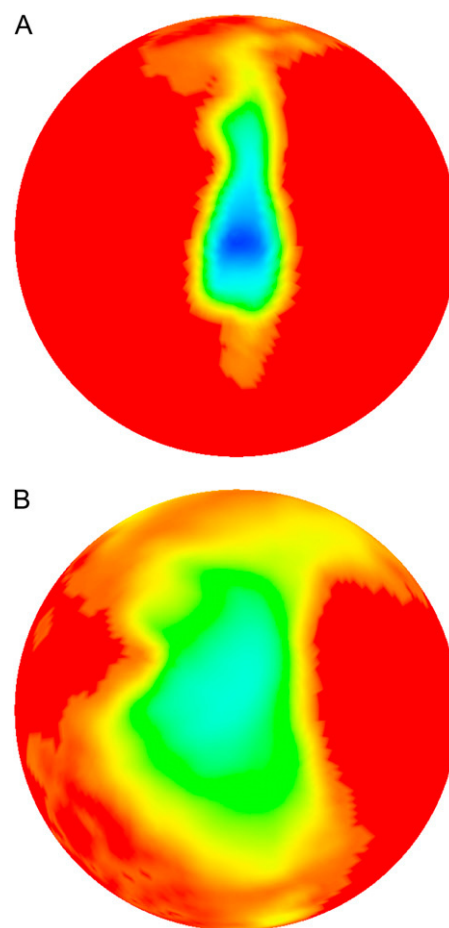
are comparable. These facts are consistent with the conclusion in the previous section that both the ionic strength and the redox state of the ferredoxin have only a modest influence on the shape of the free energy surface. The exception is BD42_{R/O} at 50 mM ionic strength. Compared with the free energy minima at 150 mM, the free energy minima at 50 mM are significantly lower: 4.5 kcal/mol lower for BD42_R and 3.9 kcal/mol lower for BD42_O. This change is caused by the greater electrostatic repulsion between the residues Asp_H^5 and Glu_F^{93} at 150 mM ionic strength. However, the locations of the free energy minima still remain the same.

Molecular dynamics simulations of encounter complexes

From the occupancy landscape and free energy landscape analyses, we identified several important encounter complexes, which are summarized in Table 2. We then used atomistic MD simulations to study the association dynamics of these encounter complexes. The average and minimum values of the edge-to-edge distances during the simulations were calculated (Table 3). The ligating residues chosen to calculate distances were those closest to one another during
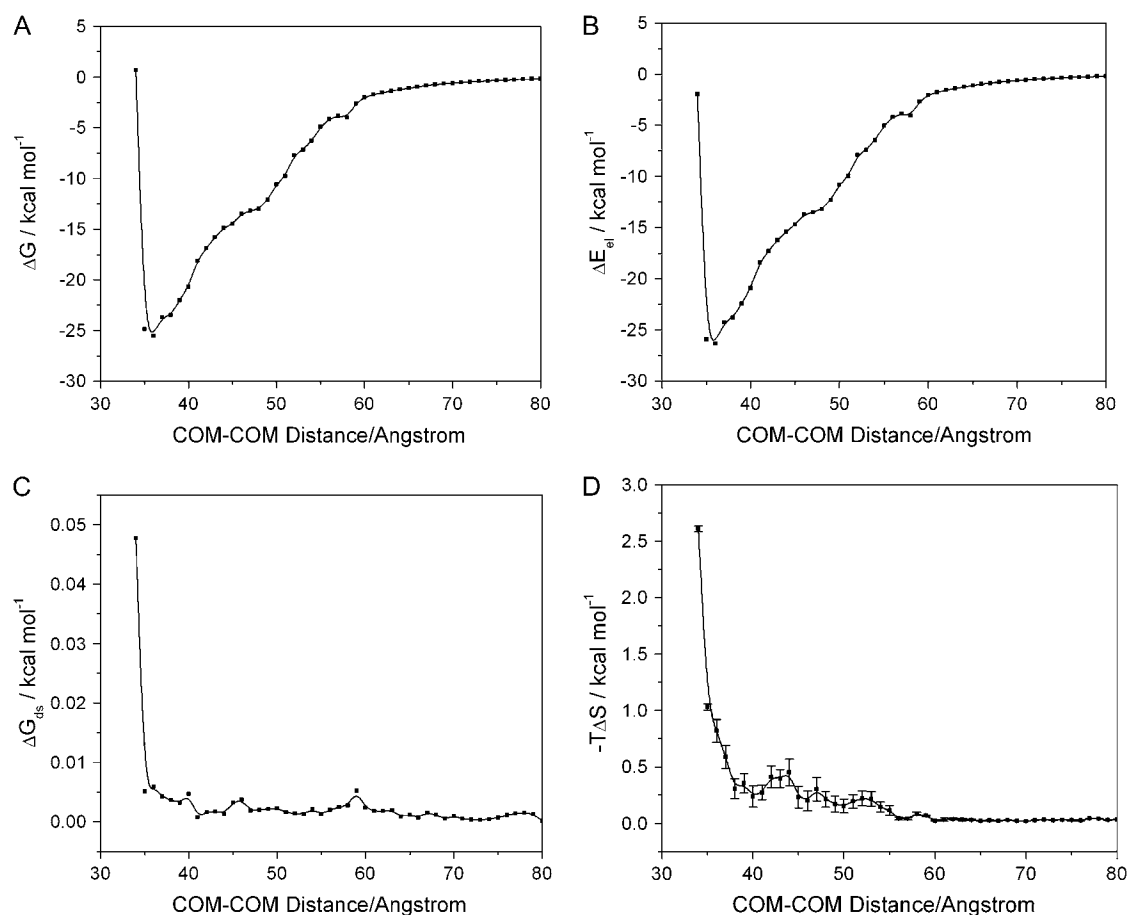
FIGURE 8 (A) Free energy curve along the reaction path for $BD16_R$ at 50 mM ionic strength. (B) Contributions from the electrostatic potential energy term. (C) The desolvation energy term. (D) The entropy term.

the MD simulations. For the A set of configurations, these were the thiolates of residues Cys_H^{366} and Cys_F^{39}, whereas for the B and C sets of configurations, the edge-to-edge distances are estimated between the thiolates of residues Cys_H^{366} and Cys_F^{39}, Cys_F^{44}, or the $[2Fe2S]_F$ cluster as noted in Table 3. All configurations with minimum edge-to-edge distances of <10 Å involve the thiolates on Cys_H^{366} and Cys_F^{39}, suggesting the potential importance of these two groups in the electron transfer process.

For the A set of configurations, the average edge-to-edge distances are all <8.2 Å, and minimum edge-to-edge distances between the iron-sulfur clusters are all <6.9 Å. The bound configurations with the reduced ferredoxin have larger edge-to-edge distances than those with the oxidized ferredoxin, which may be due to the greater negative charge on the reduced ferredoxin resulting in stronger electrostatic repulsion between the ferredoxin $[2Fe2S]_F$ and hydrogenase $[4Fe4S]_H$ clusters. This cluster-focused effect on the bound encounter complexes is opposite to the discussion mentioned above for the overall charges and protein interfaces of the oxidized versus reduced BD16/42 (see "Concluding Remarks", below). $EC42A_{R/O}$ has slightly smaller edge-to-edge distances than $EC16A_{R/O}$. The complex with the closest

edge-to-edge distance is $EC42A_O$, with 6.6 Å for the average distance and 5.4 Å for the minimum distance. For the B and C sets of configurations, the edge-to-edge distances are usually much larger, with average edge-to-edge distances of ~12–15 Å and minimum edge-to-edge distances of ~10–13 Å.

$EC16B_R$ is somewhat exceptional. In other configurations, the edge-to-edge distances are relatively stable during the simulation, which can be seen from the small standard deviation (<0.7 Å). The edge-to-edge distance of $EC16B_R$, however, drops gradually during the 3-ns simulation from >15 Å to <11 Å (Fig. 10). For this reason, we extended the simulation of $EC16B_R$ for another 1 ns and found the edge-to-edge distance stabilized around 10 Å. The simulation trajectory shows that after the 3-ns simulation, the ferredoxin rotates ~90°, turns to a configuration similar to the bound state of complex 42, and stays around this configuration for the next 1 ns of simulation (Fig. 11). Further analysis indicates that in this configuration a new salt bridge forms between Arg_H^{168} and Glu_F^{29}, which is observed neither in the original $EC16B_R$ nor in the bound state of complex 42. The formation of this salt bridge may be the driving force for the ferredoxin rotation during the MD. The minimum and average edge-to-edge distances within the fourth nanosecond
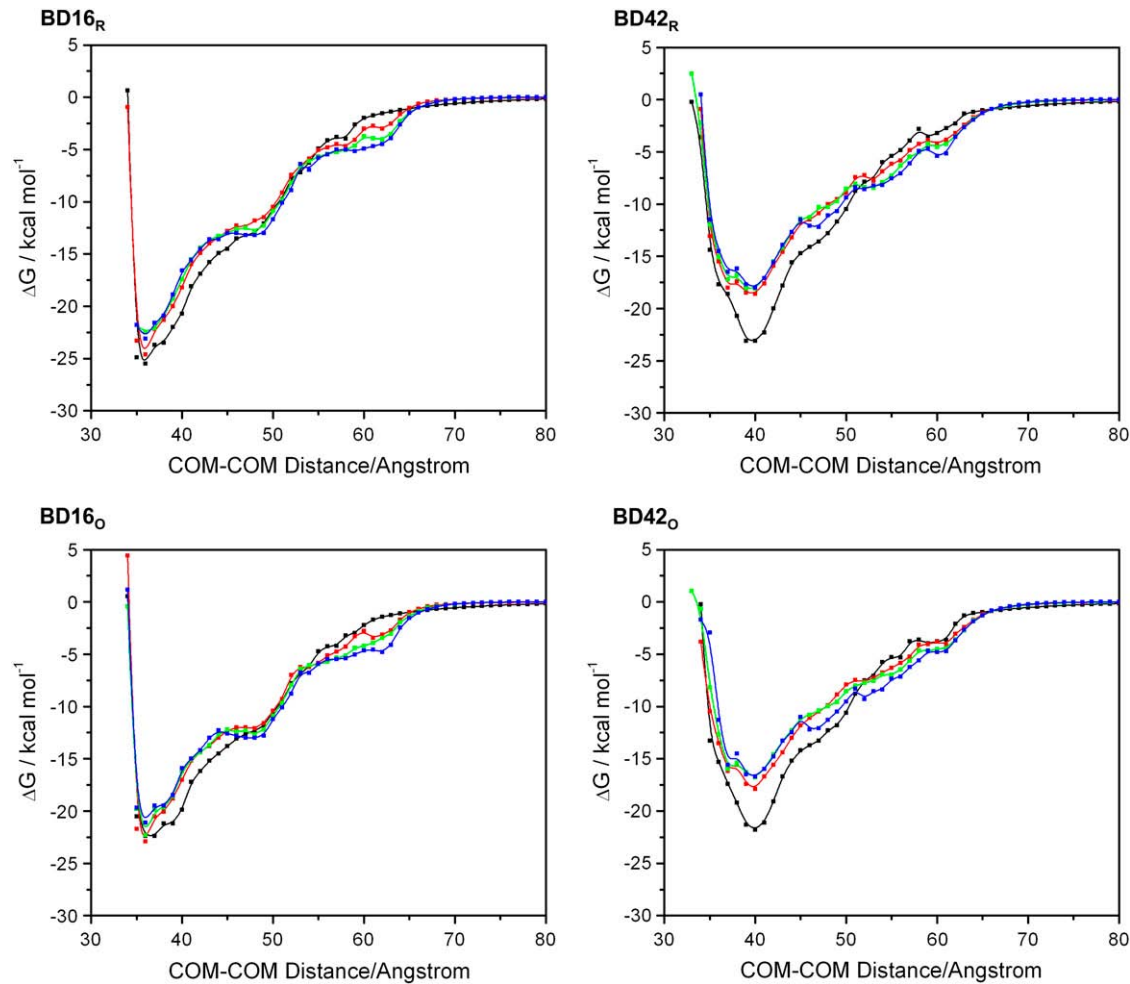
FIGURE 9   Free energy curves along the reaction path under different ionic strengths: 50 mM ionic strength (*black*), 150 mM (*red*), 300 mM (*green*), and 500 mM (*blue*). The error bars are too small to show.

of simulation were 8.9 Å and 10.4 Å, respectively, 2.0–2.2 Å larger than the values of EC16A$_R$, and 2.6–2.8 Å larger than the values of EC42A$_R$. Since the electron transfer rate depends exponentially on the edge-to-edge distance between the electron donor and acceptor (63), with the exponential decay coefficient $\beta = 1.1 \sim 1.4$ Å^{-1} for proteins (64,65), the electron transfer rate for EC16B$_R$ is predicted to be approximately one-tenth the rate of EC16A$_R$ or EC42A$_R$, indicating that the configuration EC16B$_R$ may also be important to the electron transfer active ensemble.

CONCLUDING REMARKS

By analyzing the results from BD simulations and MD simulations, we have gained insight into the hydrogenase-ferredoxin association process. The ferredoxin binds with the hydrogenase mainly via electrostatic interactions between the binding surfaces on the two proteins (18,21), resembling the binding of ferredoxin to other metabolic partners (66). When the two proteins are closer, the spatial occupancy landscapes show only one minimum, but the orientational occupancy

TABLE 3   Average and minimum edge-to-edge distances from MD simulations

Encounter complex	Average distance	Minimum distance	Encounter complex	Average distance	Minimum distance
EC16A$_R$	8.2 ± 0.4	6.9 (S in Cys$_F^{39}$)	EC16A$_O$	6.7 ± 0.5	5.5 (S in Cys$_F^{39}$)
EC16B$_R$	10.4 ± 0.4*	8.9 (S in Cys$_F^{39}$)	EC16B$_O$	13.8 ± 0.6	11.7 (S1 in FS2$_F$)
EC42A$_R$	7.6 ± 0.4	6.3 (S in *Cys$_F^{39}$*)	EC42A$_O$	6.6 ± 0.4	5.4 (S in Cys$_F^{39}$)
EC42B$_R$	13.2 ± 0.7	11.4 (S in Cys$_F^{44}$)	EC42B$_O$	12.6 ± 0.7	10.7 (S in Cys$_F^{39}$)
EC42C$_R$	15.0 ± 0.7	12.8 (S in Cys$_F^{44}$)	EC42C$_O$	12.9 ± 0.7	11.0 (S in Cys$_F^{44}$)

Minimum values are between the thiolate on Cys$_H^{366}$ and the specified thiolate of the ferredoxin indicated in the table. All distance values are in angstroms.
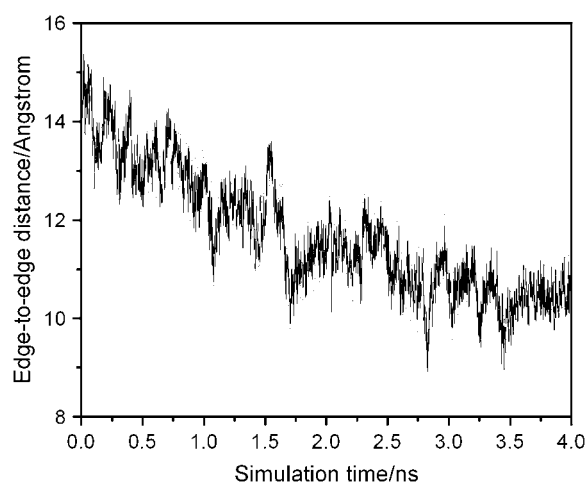*Averaged within the fourth nanosecond of simulation.

FIGURE 10 Edge-to-edge distance during the 4-ns MD simulation for EC16B$_R$.

landscapes have multiple minima. This fact indicates that the hydrogenase has only one binding surface for the ferredoxin, whereas the ferredoxin can bind to the hydrogenase in multiple orientations, using binding surfaces other than the ones used in the reference bound structures. The similarity between the EC16B$_{R/O}$ and EC42C$_{R/O}$ also reveals a new possible bound configuration besides the configurations of complexes 16 and 42.

We also identified several important encounter complexes from the BD simulation results. The encounter complexes with the minimum edge-to-edge distances (A set) are good candidates for the overall electron transfer ''transition state''—a configuration that is ready for the transfer of electrons between the two proteins because of the proximity of the respective iron clusters. Nevertheless, the encounter complexes with the lowest free energy are also important (B set), although these configurations have larger edge-to-edge distances. This means that the ferredoxin may stay around these configurations longer, providing enough time for it to reorient itself and finally evolve into a configuration with a closer edge-to-edge distance that facilitates electron transfer. If we assume that for the hydrogenase-ferredoxin association process, the binding equilibrium constant is $\sim 1/K_M$, using the experimentally measured K_M values (10 $\sim$ 35 μM (20,21)),

we can obtain a binding free energy of ~ -6 to -7 kcal/mol. This is significantly higher than the free energy values presented in Table 2. However, it should be noted that the free energy values in Table 2 are the energies for certain states during the association process. They are different from the binding free energies, which are the thermodynamic averages of all possible binding states.

When comparing our two reference model complexes, the edge-to-edge distance for EC16A$_R$ is 0.6 Å larger than the values of EC42A$_R$ on average, and 0.6 Å above the global minimum value for all the calculated ensembles (Table 3). This implies a slightly larger electron transfer rate for EC42A$_R$ compared to EC16A$_R$. However, EC42A$_R$ has a free energy 5.5 kcal/mol higher than EC16A$_R$ (Table 2), indicating that EC16A$_R$ is more likely to occur than EC42A$_R$. In addition, EC16B$_R$ can turn into an EC42A$_R$-like configuration. The edge-to-edge distances of EC16B$_R$ are 2 $\sim$ 3 Å larger than those of EC42A$_R$, resulting in an electron transfer rate $\sim$1 order of magnitude lower than that estimated for EC42A$_R$. Considering all these factors, we conclude that kinetically, the bound-state complex 16 is a better reference structure than 42. This is consistent with the conclusion in our previous thermodynamic study (31).

We studied the interactions between the oxidized hydrogenase and the reduced/oxidized ferredoxin. Liu et al. proposed that after the first electron is transferred to the H-cluster, one proton from water is then attached to the [2Fe]$_H$ cluster to neutralize this electron, so that the [2Fe]$_H$ turns into a semireduced state [2Fe(H)]$_H$ (67). The oxidized ferredoxin then dissociates. Since the ferredoxin PetF1 can only carry one electron, another cycle of reduced ferredoxin binding, electron transfer, and oxidized ferredoxin release is needed to supply a second electron to the H-cluster. The fully reduced H-cluster can then generate one hydrogen molecule. One interesting finding from our partial charge calculations is that the partial charge on the hydrogen atom in the semireduced [2Fe(H)]$_H$ cluster is close to 0, whereas the partial charges for the other [2Fe(H)]$_H$ atoms are very similar to their charges in the oxidized state [2Fe]$_H$ (manuscript in preparation). Therefore, the electrostatic potential around the semireduced, protonated H-cluster is very close to that around the oxidized cluster. Thus, one can imagine that the BD simulation results with the semireduced hydrogenase might also be very close to
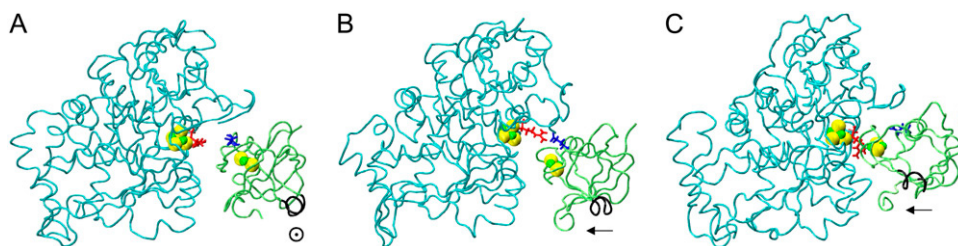

FIGURE 11 (A) Original configuration of EC16B$_R$. (B) Configuration after 3-ns MD simulation (C) Configuration of complex 42 in the bound state. The direction of a helix (black tube) in the lower right corner of the ferredoxin is shown for better comparison of these structures. The rotation mentioned in the text can be easily spotted by monitoring the direction of this helix. Residues Arg$_H^{168}$ (red) and Glu$_F^{29}$ (blue), which form a salt bridge after a 3-ns MD simulation as in B, are also shown.

our BD simulation results with the oxidized hydrogenase. For the same reason, the MD simulation results of the oxidized and semireduced hydrogenase may also be similar. This means that our results may also reflect the binding event between the reduced ferredoxin and semireduced hydrogenase leading up to H_2 generation.

Under the same conditions, the difference between the reduced and oxidized ferredoxin is subtle. The edge-to-edge distance during the MD simulation favors the oxidized ferredoxin, because of the weaker charge repulsion between the two negatively charged clusters ($[4Fe4S]_H$ in the hydrogenase and $[2Fe2S]_F$ in the ferredoxin) in the oxidized state. Nevertheless, the chance of the electron transferring back from the semireduced hydrogenase to the ferredoxin is small if electron transfer is associated with concomitant binding of a proton to the H-cluster. On the other hand, thanks to the less negative charge on the oxidized $[2Fe2S]_F$ cluster model considered here, the negative charge on the binding surface of the oxidized ferredoxin is smaller, resulting in a weaker electrostatic interaction between the ferredoxin and the positively charged surface of hydrogenase, and a higher minimum protein-protein association free energy than for the reduced form. Thus, the oxidized ferredoxin is less attractive at medium interprotein distances, but also less repulsive in the tightly bound forms, with the opposite argument true for the reduced ferredoxin. This situation serves to promote association of the reduced ferredoxin with hydrogenase while favoring the hydrogenase-ferredoxin complex form after electron transfer (and neutralization by a proton on the hydrogenase).

A potential source of uncertainty is the accuracy of our model structures. We have used homology-modeled structures from previous works (29,31) since there is no experimental structure available for the *C. reinhardtii* hydrogenase-ferredoxin binding complex or either individual protein participant. Given that these structures were stable during the 3- to 4-ns MD simulations in this research and in our previous research (31), we believe that these structures are representative of physical structures for the hydrogenase-ferredoxin binding complex, and that the results derived from these structures are meaningful for future research on the catalytic mechanism of *C. reinhardtii* HydA2.

In summary, this work uses BD and MD simulations to study the association dynamics of [FeFe] hydrogenase HydA2 and [2Fe2S] ferredoxin PetF1 from *C. reinhardtii*. BD simulation can sample the rigid-body translational and rotational phase space thoroughly and efficiently, and the resulting occupancy and free energy landscape analysis then provides an opportunity to identify the vital encounter complexes during the protein association. Subsequent atomistic MD simulations of these complexes then show the details of the protein reorientation in the final steps of the binding process. This combination of BD and MD methods provides a complementary picture of the ferredoxin-hydrogenase association dynamics. We find that the ferredoxin can bind the hy-

drogenase in multiple orientations, and encounter complexes with the minimum metallocluster edge-to-edge distance are good candidates for the ''transition state'' configuration for electron transfer. Further analysis of the MD simulation results confirms that bound-state complex 16 is a good reference structure for PetF1:HydA2 binding. Finally, the results present a more detailed picture of hydrogenase and ferredoxin association dynamics and provide a basis for evaluation of in silico mutations on the hydrogenase and ferredoxin association, with potential future improvements in photobiological hydrogen generation in *Chlamydomonas reinhardtii*.

SUPPLEMENTARY MATERIAL

To view all of the supplemental files associated with this article, visit www.biophysj.org.

REFERENCES

1. Weaver, P. F., S. Lien, and M. Seibert. 1980. Photobiological production of hydrogen. *Sol. Energy.* 24:3–45.

2. Happe, T., A. Hemschemeier, M. Winkler, and A. Kaminski. 2002. Hydrogenases in green algae: do they save the algae's life and solve our energy problems? *Trends Plant Sci.* 7:246–250.

3. Melis, A., M. Seibert, and T. Happe. 2004. Genomics of green algal hydrogen research. *Photosynth. Res.* 82:277–288.

4. Prince, R. C., and H. S. Kheshgi. 2005. The photobiological production of hydrogen: potential efficiency and effectiveness as a renewable fuel. *Crit. Rev. Microbiol.* 31:19–31.

5. Esper, B., A. Badura, and M. Rogner. 2006. Photosynthesis as a power supply for (bio-)hydrogen production. *Trends Plant Sci.* 11:543–549.

6. Rupprecht, J., B. Hankamer, J. H. Mussgnug, G. Ananyev, C. Dismukes, and O. Kruse. 2006. Perspectives and advances of biological H_2 production in microorganisms. *Appl. Microbiol. Biotechnol.* 72:442–449.

7. Ghirardi, M. L., M. C. Posewitz, P. C. Maness, A. Dubini, J. Yu, and M. Seibert. 2007. Hydrogenases and hydrogen photoproduction in oxygenic photosynthetic organisms. *Annu. Rev. Plant Biol.* 58:71–91.

8. Ghirardi, M. L., R. K. Togasaki, and M. Seibert. 1997. Oxygen sensitivity of algal H_2-production. *Appl. Biochem. Biotechnol.* 63–65:141–151.

9. Melis, A., L. P. Zhang, M. Forestier, M. L. Ghirardi, and M. Seibert. 2000. Sustained photobiological hydrogen gas production upon reversible inactivation of oxygen evolution in the green alga *Chlamydomonas reinhardtii*. *Plant Physiol.* 122:127–135.

10. Wykoff, D. D., J. P. Davies, A. Melis, and A. R. Grossman. 1998. The regulation of photosynthetic electron transport during nutrient deprivation in *Chlamydomonas reinhardtii*. *Plant Physiol.* 117:129–139.

11. Ghirardi, M. L., J. P. Zhang, J. W. Lee, T. Flynn, M. Seibert, E. Greenbaum, and A. Melis. 2000. Microalgae: a green source of renewable H_2. *Trends Biotechnol.* 18:506–511.

12. Melis, A., and T. Happe. 2001. Hydrogen production. Green algae as a source of energy. *Plant Physiol.* 127:740–748.

13. Tsygankov, A., S. Kosourov, M. Seibert, and M. L. Ghirardi. 2002. Hydrogen photoproduction under continuous illumination by sulfur-deprived, synchronous *Chlamydomonas reinhardtii* cultures. *Int. J. Hydrogen Energy.* 27:1239–1244.

14. Zhang, L. P., T. Happe, and A. Melis. 2002. Biochemical and morphological characterization of sulfur-deprived and H_2-producing *Chlamydomonas reinhardtii* (green alga). *Planta.* 214:552–561.

15. Kosourov, S., M. Seibert, and M. L. Ghirardi. 2003. Effects of extracellular pH on the metabolic pathways in sulfur-deprived, H_2-producing *Chlamydomonas reinhardtii* cultures. *Plant Cell Physiol.* 44:146–155.

16. Mus, F., L. Cournac, W. Cardettini, A. Caruana, and G. Peltier. 2005. Inhibitor studies on non-photochemical plastoquinone reduction and H_2 photoproduction in *Chlamydomonas reinhardtii*. *Biochim. Biophys. Acta..* 1708:322–332.

17. Fouchard, S., A. Hemschemeier, A. Caruana, K. Pruvost, J. Legrand, T. Happe, G. Peltier, and L. Cournac. 2005. Autotrophic and mixotrophic hydrogen photoproduction in sulfur-deprived *Chlamydomonas* cells. *Appl. Environ. Microbiol.* 71:6199–6205.

18. Florin, L., A. Tsokoglou, and T. Happe. 2001. A novel type of iron hydrogenase in the green alga *Scenedesmus obliquus* is linked to the photosynthetic electron transport chain. *J. Biol. Chem.* 276:6125–6132.

19. Jacquot, J. P., M. Stein, K. Suzuki, S. Liottet, G. Sandoz, and M. Miginiac-Maslow. 1997. Residue Glu-91 of *Chlamydomonas reinhardtii* ferredoxin is essential for electron transfer to ferredoxin-thioredoxin reductase. *FEBS Lett.* 400:293–296.

20. Happe, T., and J. D. Naber. 1993. Isolation, characterization and N-terminal amino acid sequence of hydrogenase from the green alga *Chlamydomonas reinhardtii*. *Eur. J. Biochem.* 214:475–481.

21. Roessler, P. G., and S. Lien. 1984. Purification of hydrogenase from *Chlamydomonas reinhardtii*. *Plant Physiol.* 75:705–709.

22. Kurisu, G., M. Kusunoki, E. Katoh, T. Yamazaki, K. Teshima, Y. Onda, Y. Kimata-Ariga, and T. Hase. 2001. Structure of the electron transfer complex between ferredoxin and ferredoxin-NADP$^+$ reductase. *Nat. Struct. Biol.* 8:117–121.

23. Kurisu, G., D. Nishiyama, M. Kusunoki, S. Fujikawa, M. Katoh, G. T. Hanke, T. Hase, and K. Teshima. 2005. A structural basis of *Equisetum arvense* ferredoxin isoform II producing an alternative electron transfer with ferredoxin-NADP$^+$ reductase. *J. Biol. Chem.* 280:2275–2281.

24. Jelesarov, I., A. R. Depascalis, W. H. Koppenol, M. Hirasawa, D. B. Knaff, and H. R. Bosshard. 1993. Ferredoxin binding-site on ferredoxin: NADP$^+$ reductase. Differential chemical modification of free and ferredoxin-bound enzyme. *Eur. J. Biochem.* 216:57–66.

25. Carrillo, N., and E. A. Ceccarelli. 2003. Open questions in ferredoxin-NADP$^+$ reductase catalytic mechanism. *Eur. J. Biochem.* 270:1900–1915.

26. Dorowski, A., A. Hofmann, C. Steegborn, M. Boicu, and R. Huber. 2001. Crystal structure of paprika ferredoxin-NADP$^+$ reductase: implications for the electron transfer pathway. *J. Biol. Chem.* 276:9253–9263.

27. Hurley, J. K., R. Morales, M. Martinez-Julvez, T. B. Brodie, M. Medina, C. Gomez-Moreno, and G. Tollin. 2002. Structure-function relationships in *Anabaena* ferredoxin/ferredoxin: NADP$^+$ reductase electron transfer: insights from site-directed mutagenesis, transient absorption spectroscopy and X-ray crystallography. *Biochim. Biophys. Acta.* 1554:5–21.

28. King, P. W., M. C. Posewitz, M. L. Ghirardi, and M. Seibert. 2006. Functional studies of [FeFe] hydrogenase maturation in an *Escherichia coli* biosynthetic system. *J. Bacteriol.* 188:2163–2172.

29. Forestier, M., P. King, L. P. Zhang, M. Posewitz, S. Schwarzer, T. Happe, M. L. Ghirardi, and M. Seibert. 2003. Expression of two [Fe]-hydrogenases in *Chlamydomonas reinhardtii* under anaerobic conditions. *Eur. J. Biochem.* 270:2750–2758.

30. Mus, F., A. Dubini, M. Seibert, M. C. Posewitz, and A. R. Grossman. 2007. Anaerobic acclimation in *Chlamydomonas reinhardtii*: anoxic gene expression, hydrogenase induction, and metabolic pathways. *J. Biol. Chem.* 282:25475–25486.

31. Chang, C. H., P. King, M. L. Ghirardi, and K. Kim. 2007. Atomic resolution modeling of the ferredoxin:[FeFe] hydrogenase complex from *Chlamydomonas reinhardtii*. *Biophys. J.* 93:3034–3045.

32. Humphrey, W., A. Dalke, and K. Schulten. 1996. VMD: visual molecular dynamics. *J. Mol. Graph.* 14:33–38.

33. Frey, M. 2002. Hydrogenases: hydrogen-activating enzymes. *ChemBioChem.* 3:153–160.

34. Northrup, S. H., and H. P. Erickson. 1992. Kinetics of protein protein association explained by Brownian dynamics computer simulation. *Proc. Natl. Acad. Sci. USA.* 89:3338–3342.

35. Pearson, D. C., and E. L. Gross. 1998. Brownian dynamics study of the interaction between plastocyanin and cytochrome f. *Biophys. J.* 75:2698–2711.

36. Gabdoulline, R. R., and R. C. Wade. 1997. Simulation of the diffusional association of Barnase and Barstar. *Biophys. J.* 72:1917–1929.

37. Ermakova, E. 2005. Lysozyme dimerization: Brownian dynamics simulation. *J. Mol. Model.* 12:34–41.

38. Ouporov, I. V., H. R. Knull, A. Huber, and K. A. Thomasson. 2001. Brownian dynamics simulations of aldolase binding glyceraldehyde 3-phosphate dehydrogenase and the possibility of substrate channeling. *Biophys. J.* 80:2527–2535.

39. Liang, Z. X., J. M. Nocek, K. Huang, R. T. Hayes, I. V. Kurnikov, D. N. Beratan, and B. M. Hoffman. 2002. Dynamic docking and electron transfer between Zn-myoglobin and cytochrome b(5). *J. Am. Chem. Soc.* 124:6849–6859.

40. Zollner, A., M. A. Pasquinelli, R. Bernhardt, and D. N. Beratan. 2007. Protein phosphorylation and intermolecular electron transfer: a joint experimental and computational study of a hormone biosynthesis pathway. *J. Am. Chem. Soc.* 129:4206–4216.

41. Gabdoulline, R. R., and R. C. Wade. 2002. Biomolecular diffusional association. *Curr. Opin. Struct. Biol.* 12:204–213.

42. Gabdoulline, R. R., and R. C. Wade. 2001. Protein-protein association: investigation of factors influencing association rates by Brownian dynamics simulations. *J. Mol. Biol.* 306:1139–1155.

43. Elcock, A. H., R. R. Gabdoulline, R. C. Wade, and J. A. McCammon. 1999. Computer simulation of protein-protein association kinetics: acetylcholinesterase-fasciculin. *J. Mol. Biol.* 291:149–162.

44. Tang, C., J. Iwahara, and G. M. Clore. 2006. Visualization of transient encounter complexes in protein-protein association. *Nature.* 444:383–386.

45. Camacho, C. J., Z. P. Weng, S. Vajda, and C. DeLisi. 1999. Free energy landscapes of encounter complexes in protein-protein association. *Biophys. J.* 76:1166–1178.

46. Spaar, A., C. Dammer, R. R. Gabdoulline, R. C. Wade, and V. Helms. 2006. Diffusional encounter of barnase and barstar. *Biophys. J.* 90:1913–1924.

47. Spaar, A., and V. Helms. 2005. Free energy landscape of protein-protein encounter resulting from Brownian dynamics simulations of barnase:barstar. *J. Chem. Theory Comput.* 1:723–736.

48. MacKerell, A. D., D. Bashford, M. Bellott, R. L. Dunbrack, J. D. Evanseck, M. J. Field, S. Fischer, J. Gao, H. Guo, S. Ha, D. Joseph-McCarthy, L. Kuchnir, K. Kuczera, F. T. K. Lau, C. Mattos, S. Michnick, T. Ngo, D. T. Nguyen, B. Prodhom, W. E. Reiher, B. Roux, M. Schlenkrich, J. C. Smith, R. Stote, J. Straub, M. Watanabe, J. Wiorkiewicz-Kuczera, D. Yin, and M. Karplus. 1998. All-atom empirical potential for molecular modeling and dynamics studies of proteins. *J. Phys. Chem. B.* 102:3586–3616.

49. Reed, A. E., R. B. Weinstock, and F. Weinhold. 1985. Natural population analysis. *J. Chem. Phys.* 83:735–746.

50. Meuwly, M., and M. Karplus. 2004. Theoretical investigations on *Azotobacter vinelandii* ferredoxin I: effects of electron transfer on protein dynamics. *Biophys. J.* 86:1987–2007.

51. Morales, R., M. H. Chron, G. Hudry-Clergeon, Y. Petillot, S. Norager, M. Medina, and M. Frey. 1999. Refined X-ray structures of the oxidized, at 1.3 Å, and reduced, at 1.17 Å, [2Fe-2S] ferredoxin from

the cyanobacterium *Anabaena* PCC7119 show redox-linked conformational changes. *Biochemistry.* 38:15764–15773.

52. Gordon, J. C., J. B. Myers, T. Folta, V. Shoja, L. S. Heath, and A. Onufriev. 2005. H++: a server for estimating pK(a)s and adding missing hydrogens to macromolecules. *Nucleic Acids Res.* 33:W368–W371.

53. Bashford, D., and M. Karplus. 1990. Pkas of ionizable groups in proteins: atomic detail from a continuum electrostatic model. *Biochemistry.* 29:10219–10225.

54. Gabdoulline, R. R., and R. C. Wade. 1998. Brownian dynamics simulation of protein-protein diffusional encounter. *Methods.* 14:329–341.

55. Baker, N. A., D. Sept, S. Joseph, M. J. Holst, and J. A. McCammon. 2001. Electrostatics of nanosystems: application to microtubules and the ribosome. *Proc. Natl. Acad. Sci. USA.* 98:10037–10041.

56. Gabdoulline, R. R., and R. C. Wade. 1996. Effective charges for macromolecules in solvent. *J. Phys. Chem.* 100:3868–3878.

57. de la Torre, J. G., M. L. Huertas, and B. Carrasco. 2000. Calculation of hydrodynamic properties of globular proteins from their atomic-level structure. *Biophys. J.* 78:719–730.

58. OpenDX (http://www.opendx.org).

59. Phillips, J. C., R. Braun, W. Wang, J. Gumbart, E. Tajkhorshid, E. Villa, C. Chipot, R. D. Skeel, L. Kale, and K. Schulten. 2005. Scalable molecular dynamics with NAMD. *J. Comput. Chem.* 26:1781–1802.

60. Martyna, G. J., D. J. Tobias, and M. L. Klein. 1994. Constant-pressure molecular-dynamics algorithms. *J. Chem. Phys.* 101:4177–4189.

61. Feller, S. E., Y. H. Zhang, R. W. Pastor, and B. R. Brooks. 1995. Constant-pressure molecular-dynamics simulation: the Langevin piston method. *J. Chem. Phys.* 103:4613–4621.

62. Alsallaq, R., and H. X. Zhou. 2007. Energy landscape and transition state of protein-protein association. *Biophys. J.* 92:1486–1502.

63. Marcus, R. A., and N. Sutin. 1985. Electron transfers in chemistry and biology. *Biochim. Biophys. Acta.* 811:265–322.

64. Moser, C. C., J. M. Keske, K. Warncke, R. S. Farid, and P. L. Dutton. 1992. Nature of biological electron transfer. *Nature.* 355:796–802.

65. Gray, H. B., and J. R. Winkler. 2005. Long-range electron transfer. *Proc. Natl. Acad. Sci. USA.* 102:3534–3539.

66. García Sanchez, M. I., C. Gotor, J. P. Jacquot, M. Stein, A. Suzuki, and J. M. Vega. 1997. Critical residues of *Chlamydomonas reinhardtii* ferredoxin for interaction with nitrite reductase and glutamate synthase revealed by site-directed mutagenesis. *Eur. J. Biochem.* 250:364–368.

67. Liu, Z. P., and P. Hu. 2002. A density functional theory study on the active center of Fe-only hydrogenase: characterization and electronic structure of the redox states. *J. Am. Chem. Soc.* 124:5175–5182.